

Low-resistance contact in MoSe₂-based solid-state thermionic devicesMd Golam Rosul¹,² Xiaoming Wang,^{2,3} Keivan Esfarjani,^{4,5,6} and Mona Zebarjadi^{1,5,*}¹*Department of Electrical and Computer Engineering, University of Virginia, Charlottesville, Virginia 22904, USA*²*Department of Physics and Astronomy, University of Toledo, Toledo, Ohio 43606, USA*³*Wright Center for Photovoltaic Innovation and Commercialization, University of Toledo, Toledo, Ohio 43606, USA*⁴*Department of Mechanical and Aerospace Engineering, University of Virginia, Charlottesville, Virginia 22904, USA*⁵*Department of Materials Science and Engineering, University of Virginia, Charlottesville, Virginia 22904, USA*⁶*Department of Physics, University of Virginia, Charlottesville, Virginia 22904, USA* (Received 19 January 2022; revised 22 February 2022; accepted 1 March 2022; published 14 March 2022)

Solid-state thermionic structures made from layered van der Waals heterostructures have shown promising thermal-to-electrical energy conversion efficiencies theoretically. In this paper, we further study these structures using first-principles calculations combined with the Green's function method. By calculating the electron-phonon relaxation length, we confirm ballistic transport in these structures. We study the effect of the number of layers, the energy barrier, and the asymmetry of the contacts on the performance of MoSe₂-based thermionic converters. We show that the key to high-performance thermionic diodes is to make a low-energy barrier and low-resistance metallic contacts, and we identify copper as the optimum metallic contact to MoSe₂-based devices. We further show that, unlike the vacuum-based thermionic diodes, asymmetry does not result in improved performance within the linearized transport theory.

DOI: [10.1103/PhysRevB.105.115412](https://doi.org/10.1103/PhysRevB.105.115412)**I. INTRODUCTION**

The advent of low-power portable and wearable electronics signifies the need for mesoscale power generators and coolers [1–5]. Mechanical generators cannot be miniaturized to such scales, and hence, currently, we rely on batteries to power portable electronics. Thermionic power generators and coolers can be built with nanoscale thickness and provide a solid-state solution for energy scavenging and integrated cooling.

A thermionic converter essentially is a heat engine that converts thermal energy directly to electricity using electrons as the working fluid. Like most other heat engines, thermionic devices can operate either as power generators or coolers. There are two main types of thermionic converters: vacuum state thermionic converters (VSTICs) and solid-state thermionic converters (SSTICs) [1,2,6–8]. In the power generation mode, heat is used to increase the energy of electrons in the cathode. The hot electrons with energies higher than the energy barrier can pass above the barrier with a Richardson flux. These electrons are then collected by a colder anode. A part of the thermal energy is thus converted directly to electricity, and the rest is rejected as heat to the cold side. The energy barrier in the case of VSTIC is the cathode work function, which is on the order of a few electron volts in typical metals. Therefore, VSTICs can only operate at very high temperatures. Also, the need for a vacuum in a VSTIC restricts direct access to the electrodes. To overcome these difficulties, Shakouri and Bowers [1] proposed a single-layer SSTIC in

which the vacuum is replaced by a semiconducting material. In this structure, the semiconductor layer is the energy barrier that an electron experiences. Mahan proposed the idea of using multilayer barriers in which each layer maintains a small temperature difference [2,7]. Electrons in an SSTIC can face an effective energy barrier height on the order of millielectronvolts as the energy barrier is the difference between the electron affinity of the semiconductor and the work function of the metal. This is compared with a few electronvolt barrier heights in a VSTIC. Hence, SSTICs can operate at much lower temperatures than VSTICs. Our previous theoretical work focusing on the mathematical optimization of SSTICs concluded that, for optimum performance, the optimum barrier height should be on the order of a few $k_B T$ where k_B is the Boltzmann constant and T is the temperature [8].

The transport inside the semiconducting layer of an SSTIC must be ballistic to avoid electron-phonon thermalization. To maintain ballistic transport in an SSTIC, the semiconducting layer thickness should be lower than the electron mean-free path (MFP). At the same time, a minimum barrier thickness is needed to suppress the tunneling of electrons in the device. If electrons of energy lower than the semiconductor barrier height tunnel through, they carry less energy if their energy is above the Fermi level and will carry negative heat (a rare event) if their energy is below the Fermi level. This leads to a lower Seebeck coefficient, as our previous and present studies have shown. Hence, SSTICs are considered nanoscale devices appropriate for integrated circuits [6,9,10]. At such small scales, the main challenge of SSTICs is their thermal leakage [11]. To maintain a noticeable temperature difference at such a small length scale, the thermal conductance of an SSTIC needs to be very

*Corresponding author: mz6g@virginia.edu

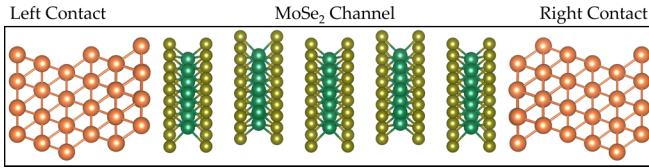


FIG. 1. Ball-stick model of a metal-MoSe₂-metal device configuration.

small. Our recent work has shown that the thermal conductance of an SSTIC should be $<0.1 \text{ MW m}^{-2} \text{ K}^{-1}$ to obtain reasonable efficiencies [8]. To our best knowledge, within ordered and nonporous systems, this very small thermal conductance is only possible in the van der Waals (vdW) heterostructures [12,13] due to their weak vdW interactions compared with covalent bonding [14]. In one work, our group showed that five layers of black phosphorene sandwiched between gold and graphene has a thermal conductance value of $4\text{--}6 \text{ MW m}^{-2} \text{ K}^{-1}$ [15]. In another work, our group theoretically calculated a thermal conductance value of $16 \text{ MW m}^{-2} \text{ K}^{-1}$ for a Sc-WSe₂-MoSe₂-WSe₂-Sc structure [16]. Other weakly bonded structures also demonstrated extremely low thermal conductance values. It was shown that interfacial thermal conductance between seven layers of MoS₂ and crystalline silicon (c-Si) is $<1 \text{ MW m}^{-2} \text{ K}^{-1}$ [17]. In another work, it was experimentally shown that $5\text{--}10 \text{ MW m}^{-2} \text{ K}^{-1}$ thermal conductance can be obtained in the vdW structure [18]. A theoretical work based on molecular dynamics simulation obtained a slightly higher thermal conductance value of $17 \text{ MW m}^{-2} \text{ K}^{-1}$ for both graphene-WSe₂-graphene and graphene-MoSe₂-graphene structures. In another experimental work, a very low thermal conductance value of $0.5 \text{ MW m}^{-2} \text{ K}^{-1}$ was estimated for a graphene-WSe₂-graphene structure [19]. In addition, in a vdW heterostructure, the barrier height, which plays a significant role in improving the device performance, can be tuned by changing the number of layers in the heterostructure from zero in the tunneling regime (one layer) to the bulk bandgap value for a large enough number of layers (typically 10 layers) [15]. In recent years, these two important features of vdW heterostructures have renewed interest in SSTICs [5,15,16,20–22].

In this paper, we study thermionic transport properties of a metal-MoSe₂-metal structure, as shown in Fig. 1, by using density functional theory (DFT)-based first-principles calculations combined with real-space Green's function (GF) transport formalism. MoSe₂, a layered two-dimensional (2D) transition metal dichalcogenide (TMD), is used as the semiconducting material in these calculations. An advantage of layered TMD materials such as MoSe₂ is that the saturated covalent bonds within one layer and noncovalent binding between the layers allow for atomically sharp and stress-free interfaces between similar or dissimilar materials [23]. Another important feature of MoSe₂ is that the electronic properties depend on the number of layers. For example, bulk MoSe₂ has an indirect bandgap of 0.85 eV, while monolayer MoSe₂ has a direct bandgap of 1.55 eV [24,25]. Moreover, the thermal transport in MoSe₂ in the cross-plane direction is greatly reduced due to the lack of covalent bonding between

layers. These electrical and thermal properties make MoSe₂ a suitable material for designing efficient SSTICs.

In nanoscale electronics, contacts often play a more important role than the semiconducting material itself [26,27]. While contact in Si-based devices is no longer challenging after many years of engineering optimization, contact to nanoscale electronic devices based on 2D TMD materials has become a major challenge [28–31]. A strong interface bonding creating interface states that pin the Fermi level [32] or a weak bonding creating a potential step due to Pauli repulsion [33,34] at the interface can cause high barrier height between the metal contact and the 2D TMDs. Therefore, for the applicability of 2D TMDs such as MoSe₂ as nanoscale devices, a comprehensive study of metal contacts to the 2D TMDs is very important. There are several ways to extract the metal-2D TMD barrier height [35]. In this paper, we extract the barrier height between metal-MoSe₂ from the electronic transmission function. We first systematically study the contact between MoSe₂ and various metals (Au, Pt, Ni, and Cu). We then study thickness dependence of the contact and identify ohmic contacts. We also study the thermionic performance of these structures.

Next, we investigate the effect of asymmetric metallic contact on the performance of SSTICs. In a VSTIC, the output power is proportional to the work function difference between the cathode and the anode. Hence, it is desired to have asymmetric electrodes wherein the cathode has a larger work function than the anode [36–38]. The SSTICs designed so far have similar metallic contact as cathode and anode [5,15,16]. Therefore, the effect of asymmetric metallic contact with different work functions on the device performance is unknown. In this paper, we evaluate the performance of two sets of asymmetric structures (Au-MoSe₂-Pt and Cu-MoSe₂-Au) and compare their performance with their symmetric counterparts (Au-MoSe₂-Au, Pt-MoSe₂-Pt, and Cu-MoSe₂-Cu).

II. COMPUTATIONAL METHOD

A. DFT calculation details

To model the proposed device, we use open boundary conditions along the z axis, while periodicity is imposed in the xy plane. To study the structural and electronic properties of the metal₁-MoSe₂-metal₂ vdW heterostructure, we used the state-of-the-art DFT-based first-principles calculations combined with real-space GF transport formalism, as implemented in the SIESTA package [39]. We used the exchange-correlation functional of Perdew-Burke-Ernzerhof (PBE) [40] revised for solids [41] and standard basis set, namely, double zeta plus polarization. Real-space mesh cutoff energy was set to 300 Ry. A single k point in the cross-plane direction whereas a $5 \times 5k$ mesh in the basal plane was used for the Brillouin zone sampling.

B. Making and optimization of the SSTICs

We first optimized the lattice parameters of Au, Pt, Cu, Ni, and MoSe₂ separately for the purpose of obtaining the optimized in-plane lattice parameters of the structures. The optimized in-plane lattice constants are 4.08, 3.93, 3.61, 3.52, and 3.31 Å, respectively. Our calculated in-plane lattice

parameter of MoSe₂ matches the reported value in the literature [16,42–44]. Therefore, the in-plane lattice parameters of the relaxed ⟨111⟩ plane of the metallic contacts (Au, Pt, Cu, and Ni) are 2.885, 2.779, 2.553, and 2.489 Å, respectively. In the structures, 3–6 layers of MoSe₂ are sandwiched between six layers of ⟨111⟩ plane of the metallic contacts. In the DFT-GF method, the electrodes are assumed to be semi-infinite, and using six layers, we achieved convergence in the results. The transport properties will not change when the number of layers of the metallic contact increased beyond six. The in-plane lattice parameters of the structures are fixed to the optimized metal ⟨111⟩ plane for the symmetric structures, while the average of the relaxed metal₁ ⟨111⟩ plane and the relaxed metal₂ ⟨111⟩ plane for asymmetric structures and in-plane MoSe₂ lattice parameters were adapted accordingly ($2\sqrt{3}a_{\text{Au/Pt}\langle 111 \rangle} = 4a_{\text{Cu/Ni}\langle 111 \rangle} = 3a_{\text{MoSe}_2}$, where a is the lattice constant) to minimize the strain. Thus, the MoSe₂ in the Au-MoSe₂-Au, Pt-MoSe₂-Pt, Cu-MoSe₂-Cu, Ni-MoSe₂-Ni, Au-MoSe₂-Pt, and Au-MoSe₂-Cu structures experience 0.65% tensile, 3% compressive, 2.8% tensile, 0.26% tensile, 1.24% compressive, and 1.73% tensile strain, respectively. It is known that the tensile strain increases the bandgap, while the compressive strain decreases it [45,46]. After forming the devices, all structures are optimized again. In the optimization process, the atomic positions of two inner layers of metal from each side along with all the MoSe₂ layers, called the *channel region*, are allowed to relax without any constraints along the cross-plane direction until the forces on all atoms are <0.01 eV/Å, while the atomic positions of the outer four metallic layers from each side, considered left and right contacts, are kept fixed. We use the nonlocal vdW DFT functional (vdW-DF-optb86) [47,48] to correctly consider the vdW interaction during the structure optimization.

C. Electron transport calculations

The electronic transport properties of the SSTICs are studied by using DFT-based first-principles calculations combined with real-space GF transport formalism. The transport properties calculations of the optimized structures are performed using PBE functionals. Although a generalized gradient approximation functional such as PBE used in this paper underestimates the bandgaps, due to the presence of two metallic electrodes which strongly screen the Coulomb interaction, the bandgap becomes small so that we have a cancellation of this underestimation error. This was confirmed in our previous work by comparing with the GW calculations on the same structure [16]. The electron transmission functions are calculated using the real-space GF method as in the TRANSIESTA implementation [49]. TRANSIESTA deals fully with the atomistic structure of the whole system, treating both the contact and the electrodes on the same footing. After calculating the electron transmission function using TRANSIESTA, the transport coefficients are obtained using the linear response approximation [50]:

$$\text{Conductance, } G = q^2 L_0,$$

$$\text{Seebeck coefficient, } S = L_1 / q T L_0,$$

$$\text{Electronic thermal conductance, } \kappa_{el} = (L_2 - L_1^2 / L_0) / T,$$

$$\text{where } L_n = 2/h \int dE T(E) (E - \mu)^n \left(-\frac{\delta f}{\delta E}\right),$$

where q is the electron charge, and f is the Fermi-Dirac distribution function.

D. Electron-phonon scattering rate and MFP calculation

We compute the electron-phonon scattering rate and the MFPs in bulk MoSe₂ using the first principles. The equilibrium properties of electrons and phonons are calculated using the DFT and density functional perturbation theory (DFPT) as implemented in the QUANTUM ESPRESSO package [51]. The norm-conserving pseudopotentials [52] with the PBE [40] functional for the exchange-correlation are used. Here, $6 \times 6 \times 2$ and $12 \times 12 \times 4$ Monkhorst-Pack k-point meshes are used for the self-consistent and non-self-consistent field calculations, respectively, and the cutoff energy of the plane wave is chosen as 60 Ry. The convergence threshold of energy is set to be 10^{-12} Ry. Lattice was relaxed with the force convergence threshold of 10^{-4} Ry/Bohr. The obtained relaxed lattice constant of bulk MoSe₂ in the hexagonal structure are $a = b = 3.31$ Å and $c = 12.89$ Å. The dynamical matrices and phonon perturbations are computed on a $6 \times 6 \times 2$ q-point mesh in the phonon calculations. To obtain the electron-phonon scattering rates, the EPW package [53] is employed to interpolate the electron-phonon coupling matrices as well as electron and phonon eigenvalues obtained by DFT and DFPT calculations from coarse to fine k- and q-point meshes ($30 \times 30 \times 30$) using the Wannier interpolation scheme [54]. The electron group velocities are obtained from the BOLTZTRAP package [55]. Finally, the MFP is obtained by multiplying the electron-phonon scattering rates with the group velocities.

III. RESULTS AND DISCUSSION

A. Metallic contact for MoSe₂ based electronics

Today, many 2D layered materials are identified. Monolayers can be peeled off and stacked on top of each other to form a variety of desired thermal, optical, and electronic properties, opening the possibility of nanoscale electronic devices for a variety of medical, environmental, security, and sensing applications. A challenge to make the desired planar electronics out of these Lego-type stacked layers is the formation of low-resistance metallic contacts. The contact resistance and particularly the potential barrier height are important parameters for thermionic transport as well as making metallic contact in a 2D planar device consisting of TMD materials. To form low-resistance contact between the metal and the 2D TMD materials, the potential barrier height needs to be very low (on the order of $k_B T$). We calculate the potential barrier height of a metal-MoSe₂-metal SSTIC consisting of five layers of MoSe₂ for different metals (Au, Pt, Cu, and Ni) as well as a Au-MoSe₂-Au structure for 3–6 layers of MoSe₂. A simple way to estimate the potential barrier height is the Schottky-Mott (SM) rule, $E_b = I - W$ (for holes) or $E_b = W - \chi$ (for electrons), where E_b is the potential barrier height, W is the work function of the metal, I is the ionization potential of the semiconductor, and χ is the electron affinity of the semiconductor. However, this simple and approximate method does not always predict the correct potential barrier height [16] and certainly does not work well for our studied

TABLE I. Calculated bandgap and barrier height of metal-5 MoSe₂-metal SSTIC.

Metal contact	Au	Pt	Cu	Ni
5L MoSe ₂	0.89	0.89	0.87	0.80
Transmission gap (eV)				
Barrier height (eV) (calculated)	0.26	0.42	0.10	0.30
	(<i>n</i> type)	(<i>p</i> type)	(<i>n</i> type)	(<i>n</i> type)
Barrier height (eV) (SM rule)	0–0.14	0–0.12	0.62 (<i>n</i> type)	0–0.20
	(<i>p</i> type)	(<i>p</i> type)	0.14 (<i>p</i> type)	(<i>p</i> type)

structures. Here, we use a more accurate first-principles-based method to extract the potential barrier height. First, we use first-principles calculations to relax the metal-MoSe₂-metal structure. Next, we calculate the transmission function of the structure using the GF method (see Fig. S1 in the Supplemental Material [56]). We then calculate the E_b for electrons by measuring the $E_c - E_F$ for electrons and $E_F - E_v$ for holes from the transmission function, where E_F is the Fermi energy, E_c (E_v) refers to the corresponding energy levels at the start of nonzero transmission above (below) the Fermi level. As an example, the work function of gold (111) is 5.1 eV, and the ionization potential of a single layer of MoSe₂ is 5.22 eV [57]. Therefore, the SM rule predicts a barrier height of 0.12 eV and a *p*-type transport, whereas our first-principles calculation indicates a barrier height of 0.26 eV and an *n*-type transport. Similarly, the calculated barrier height is *n* type for Cu, while the SM rule predicts a *p*-type barrier height. Table I summarizes the calculated potential barrier height of a metal-5 MoSe₂-metal structure and a range of barrier heights predicted by the SM rule for Au, Pt, Cu, and Ni. The table also shows the transmission gap E_g for MoSe₂ in each structure, where $E_g = E_c - E_v$. We note that it is more difficult to extract this information from the local density of states (LDOS), as the screening effect of the metal on its adjacent layer results in a tail in the density of states; hence, we define the transmission gap instead of the bandgap. From the calculated potential barrier heights listed in the table, we see that Cu makes low-energy contact for MoSe₂, which becomes *n* type, with a barrier height of 0.10 eV. Therefore, it is expected that the Cu-MoSe₂-based SSTIC should have the highest electrical conductance among the studied metals.

Next, we study the effect of the number of MoSe₂ layers on metal-MoSe₂ contact resistance. The energy states of the metal significantly affect the energy states of the adjacent layers. This screening effect damps with distance, and hence, it is expected that the barrier height should be dependent on the number of layers. Here, we calculate the potential barrier height for a Au-MoSe₂-Au SSTIC where the number of layers of MoSe₂ varied from 3 to 6 layers in the heterostructure. Table II shows the potential barrier height for the Au-3-6MoSe₂-Au SSTIC. We see that the SSTIC with three layers of MoSe₂ shows the lowest barrier height of 0.2 eV,

 TABLE II. Variation of barrier height with the numbers of MoSe₂ layers.

Number of layers	3 layers	4 layers	5 layers	6 layers
Barrier height (eV)	0.20	0.30	0.33	0.40

which is therefore expected to show the highest electrical conductance, as more electrons will overcome the energy barrier. We note that the transmission gap closes for 1 and 2 layers, and transport is dominantly through tunneling.

Next, we evaluate the performance of the Au-3-6 MoSe₂-Au SSTICs. Figure 2(a) shows the transmission function of the structure containing 3–6 layers of MoSe₂. Figures 2(b) and 2(c) show the electrical conductance (σ) and Seebeck coefficient (S) of all the structures. The electrical conductance of the structure with three layers of MoSe₂ is maximum, and electrical conductance decreases as the number of MoSe₂ layers in the structure increases. This is consistent with the barrier height of the structures, as shown in Table II. Also, due to the increase in the number of thermally excited electrons, the electrical conductance increases as the temperature increases, as shown in Fig. 2(b). The Seebeck coefficient increases with the number of MoSe₂ layers in the heterostructure because the transmission gap increases with the number of layers. The power factor \times temperature (PFT = $\sigma S^2 T$), a parameter that is used to characterize the power generated by the SSTIC, is shown in Fig. 2(d) for all structures. The PFT is optimum for the structure with three layers of MoSe₂ at temperature ranges of 200–500 K and 970–1200 K, while structures with 4 and 5 layers of MoSe₂ show optimum PFT at temperature ranges of 500–750 K and 750–970 K, respectively. A breakdown of the PFT for

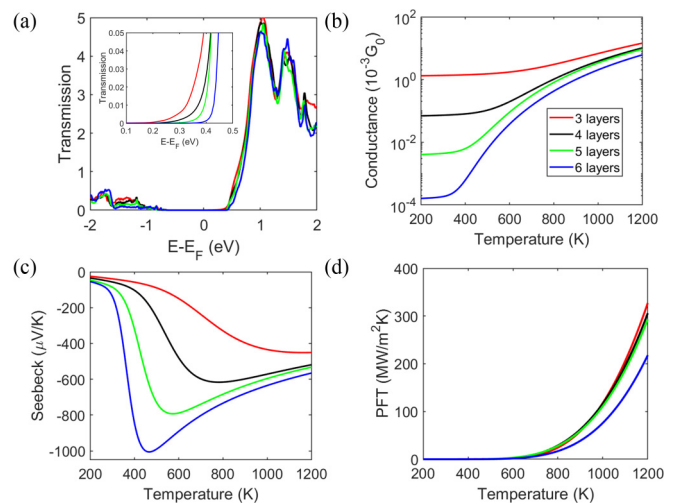


FIG. 2. (a) Transmission function, (b) electrical conductance, (c) Seebeck coefficient, and (d) power factor \times temperature of a heterostructure containing 3–6 layers of MoSe₂. The inset of figure (a) shows a closeup of the transmission functions.

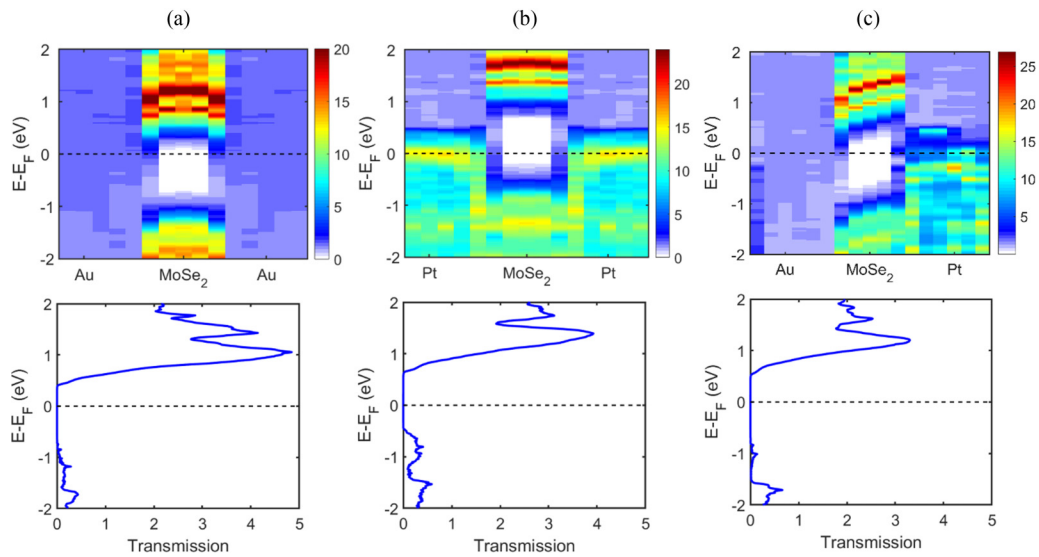


FIG. 3. Local density of states of (a) Au-5 MoSe₂-Au, (b) Pt-5 MoSe₂-Pt, (c) Au-5 MoSe₂-Pt, and their corresponding transmission functions.

each of these temperature ranges is shown in Supplemental Material Fig. S2 [56]. The maximum power factor for the structure with three layers of MoSe₂ is 327 MW m⁻² K⁻¹ at 1200 K. For comparison, our previously calculated structures Au-Gr-3WSe₂-Gr-Au and Pt-Gr-3WSe₂-Gr-Pt showed PFTs of 0.83 and 60 MW m⁻² K⁻¹, respectively, at 800 K [5], and Sc-WSe₂-3 MoSe₂-WSe₂-Sc showed a PFT of 427 MW m⁻² K⁻¹ at 1200 K [16]. Note that the unit used here is for 2D structures and is different to those used for bulk thermoelectric power factor.

B. Asymmetric MoSe₂-based SSTIC

In VSTIC, two dissimilar metals with work function differences > 1 eV are used as cathode and anode, and the output power is proportional to the work function difference between the metals. The SSTICs designed so far have similar metallic contact as cathode and anode [5,15,16]. Therefore, the effect of asymmetric metallic contact with different work functions on the device performance is not understood. In this section, we evaluate and compare the performance of two sets of symmetric and asymmetric SSTICs. In the first set of calculations, we evaluate the performance of symmetric Au-5 MoSe₂-Au, symmetric Pt-5 MoSe₂-Pt, and asymmetric Au-5 MoSe₂-Pt structures, and in the second set of calculations, we evaluate the performance of symmetric Au-3 MoSe₂-Au, symmetric Cu-3 MoSe₂-Cu, and asymmetric Au-3 MoSe₂-Cu structures. Since in the previous part we identified 3–5 layers as optimally performed devices, for all calculations in this section, 3 or 5 layers of MoSe₂ are used.

Figure 3 shows the LDOS of symmetric gold, symmetric platinum, and the asymmetric structure with one side gold and another side platinum and their corresponding transmission functions. Gold and platinum are chosen since they have similar work functions. From the LDOS, we see that the Fermi level E_F is located near the conduction band of the gold and gold-platinum asymmetric structure, which means these structures are *n* type, while the Fermi level of the platinum structure is located near the valence band, making it *p* type.

The transmission function, Seebeck coefficient, electrical conductance, and PFT for all three structures are shown in Fig. 4. As can be seen from the LDOS and the transmission function, the gold structure has a lower barrier height than the other two structures. Therefore, the gold structure shows higher electrical conductance values, as shown in Fig. 4(b). The platinum structure shows a positive Seebeck coefficient, while the gold and gold-platinum asymmetric structures show negative Seebeck coefficients [Fig. 4(c)], which is consistent with the *p*- and *n*-type barrier heights of the respective structures. The platinum structure shows a maximum Seebeck coefficient of 620 μ V/K at 620 K, while the maximum Seebeck coefficients of the gold and gold-platinum asymmetric structures

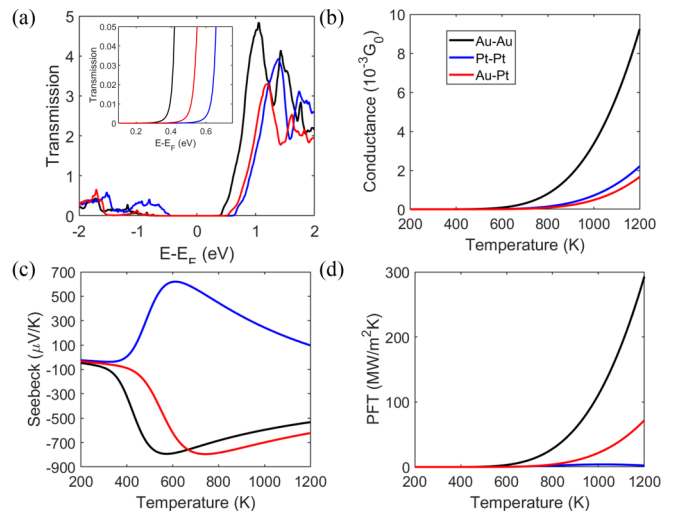


FIG. 4. (a) Transmission function, (b) electrical conductance, (c) Seebeck coefficient, and (d) power factor \times temperature of the gold, platinum, and gold-platinum asymmetric structure containing five layers of MoSe₂. The black line represents the gold structure, the blue line represents the platinum structure, and the red line represents the gold-platinum asymmetric structure. The inset of figure (a) shows a closeup of the transmission functions.

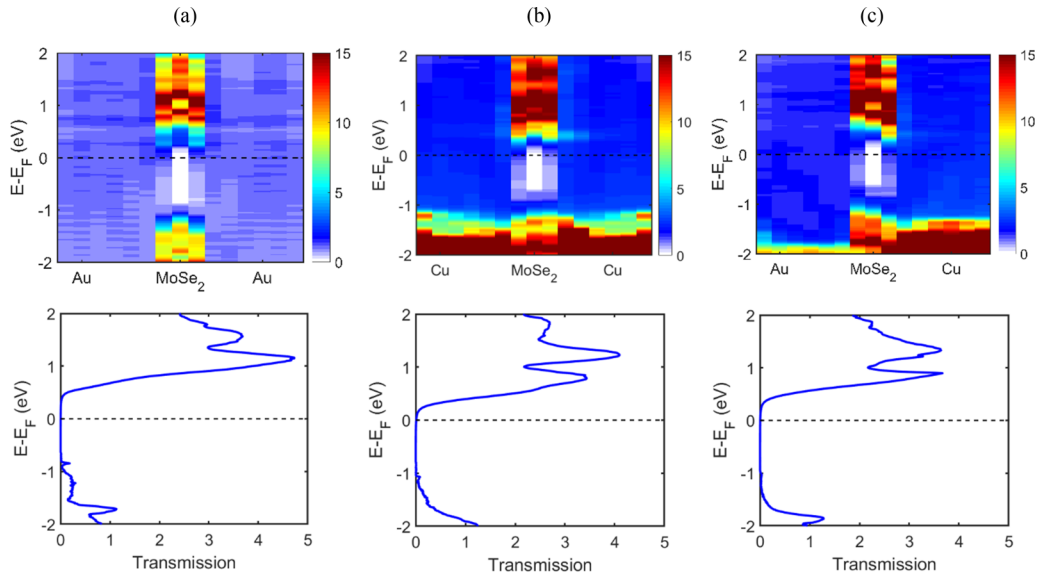


FIG. 5. Local density of states of (a) Au-3 MoSe₂-Au, (b) Cu-3 MoSe₂-Cu, (c) Au-3 MoSe₂-Cu, and their corresponding transmission functions.

are -792 and -795 $\mu\text{V}/\text{K}$ at 572 and 740 K, respectively. The presence of the bandgap in these structures contributes to the large Seebeck coefficients. The PFT of all three structures is shown in Fig. 4(d). The high electrical conductance due to low barrier height and the high Seebeck coefficient of the gold structure results in the highest PFT at high temperatures. The low electrical conductance combined with the low Seebeck coefficient makes the platinum structure the worst performing among the three structures, while the PFT of the platinum-gold asymmetric structure is in between the PFT of the gold and platinum structures.

In the previous set of calculations, we see that, while the gold and gold-platinum asymmetric structures are n type, the platinum structure is p type. For the next set of calculations, we find another metal contact that has a very close work function to gold and creates a structure that is n -type doped. We choose copper for this calculation, which has a work function value of 4.53 – 5.10 eV. Therefore, Au-3 MoSe₂-Au and Cu-3 MoSe₂-Cu are the symmetric structures, and Au-3 MoSe₂-Cu is the asymmetric structure for these calculations. The LDOS and the corresponding transmission function of symmetric gold, symmetric copper, and gold-copper asymmetric structures are shown in Fig. 5. The Fermi levels E_F for all these structures are close to the conduction band, which means all the structures are n -type doped. The energy barrier height of the copper structure is significantly lower than the other two structures. The electrical conductances of all the structures are shown in Fig. 6(b). The electrical conductance of the copper structure is very high compared with the other two structures due to the significantly lower barrier height. The n -type doping of all the structures can be further verified by the negative Seebeck coefficient, as shown in Fig. 6(c). The maximum Seebeck coefficient of the gold, copper, and gold-copper asymmetric structures are -451 , -321 , and -373 $\mu\text{V}/\text{K}$, respectively, at 1200 K. The PFT of the gold, copper, and gold-copper asymmetric structures are 327 , 917 , and 373 $\text{MW m}^{-2} \text{K}^{-1}$, respectively, at 1200 K [Fig. 6(d)]. The

PFT of the copper structure is the highest among all the SSTICs that have been calculated so far [5, 16, 58].

We note that the transport properties of the asymmetric structure are always in between the two symmetric ones. The only exception is the Seebeck coefficient in the range of 600 to ~ 1000 K, wherein the asymmetric structure shows a Seebeck coefficient smaller than both symmetric counterparts.

From these two sets of calculations, we see that the PFT of the asymmetric structure is in between the PFT of their symmetric counterpart. Although the asymmetry of the metallic contact improves the performance of VSTICs, it does not

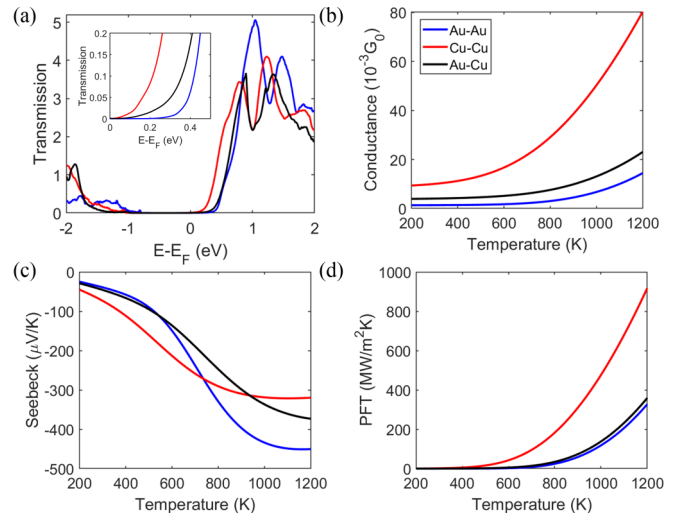


FIG. 6. (a) Transmission function, (b) electrical conductance, (c) Seebeck coefficient, and (d) power factor \times temperature of the gold, copper, and gold-copper asymmetric structure containing three layers of MoSe₂. The blue line represents the gold structure, the red line represents the copper structure, and the black line represents the gold-copper asymmetric structures. The inset of figure (a) shows a closeup of the transmission functions.

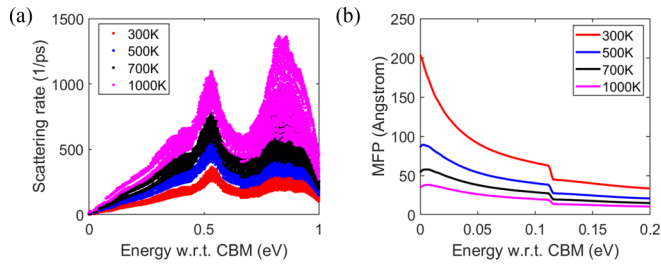


FIG. 7. (a) Electron-phonon scattering rate for bulk MoSe₂. (b) Electron mean-free path calculated along the z axis.

affect the performance of SSTICs. This is possibly due to the difference in the operating temperature and barrier height between the two types. One must keep in mind that, given the nanoscale thickness of these devices, only a very small temperature difference can be maintained between the electrodes. Since the optimal operating temperatures of symmetric structures are very different, the performance of the asymmetric structure can never be superior to the symmetric ones unless their barrier height is the same. Whereas the VSTIC barrier height is a few electronvolts, the ideal barrier height of SSTIC is only on the order of millielectronvolts. Given the small temperature difference which can be maintained in these structures, we can linearize the theory of thermionic transport and define the equivalent Seebeck coefficient and the power factor. Upon doing so, the asymmetric structure shows average properties, in between the two symmetric counterparts, like how averaging is done in thermoelectric structures. The most important parameter in these structures seems to be the barrier height itself. The lower the barrier height, the higher the power factor. We know the optimum barrier height is $\sim 2k_B T$, which corresponds to 50 meV at room temperature and 100 meV at 600 K. The latter is close to the barrier height of the Cu structure.

Finally, since we are describing electron transport using a coherent formalism and have neglected inelastic scatterings, our results are only approximate at very high temperatures where the electron MFP can become shorter than the barrier thickness. In practice, the electrical conductance and power factor should start decreasing with T at high enough temperatures. We calculated the MFP of bulk MoSe₂ along the z axis at different temperatures from first principles to estimate the effect of inelastic electron-phonon scattering on the transport properties. The energy-dependent electron-phonon scattering rates and MFP are shown in Fig. 7. The electron MFP at the bottom of the conduction band at 300 K is 200 Å and at 1000 K is 35 Å. The length of the 3 and 5 layers of MoSe₂ devices are 19.35 and 32.25 Å, respectively. Therefore, up to 1000 K, the inelastic electron-phonon scattering should not

affect the performance of the 3 and 5 layers of MoSe₂ based SSTICs.

IV. CONCLUSIONS

We used first-principles DFT combined with real-space GFs formalism to evaluate the performance of SSTICs with a varying number of MoSe₂ layers and with a variety of metallic electrodes. Among the studied metals, copper makes the lowest energy contact for electron transport, while platinum makes low energy contact for hole transport with MoSe₂. The Cu-3 MoSe₂-Cu structure shows an extremely large PFT of 917 MW m⁻² K⁻¹ at 1200 K, which is the largest power factor calculated for a thermionic structure based on TMDs. Since the barrier height can be tuned with the number of layers, we investigated the contact barrier dependence on the number of layers by studying the contact between gold and 3–6 layers of MoSe₂. We found that Au with three layers of MoSe₂ shows the lowest barrier height and, hence, makes better ohmic contact. Furthermore, we evaluated the performance of SSTICs with 3–6 layers of MoSe₂ sandwiched between two gold contacts and evaluated how their performance changes with the number of layers. Structures with 1 and 2 layers of MoSe₂ are not included, as the transport in these structures is dominated by tunneling of carriers, which is not desirable for SSTICs. We find that SSTICs with three layers of MoSe₂ show optimum performance at temperature ranges of 200–500 K and 970–1200 K, while devices with 4 and 5 layers of MoSe₂ show optimum performance at temperature ranges of 500–750 K and 750–970 K, respectively. Therefore, the number of layers can be optimized for a given target operating temperature. Next, we studied the performance of two sets of asymmetric SSTIC. Although an asymmetric metallic electrode enhances the efficiency of a VSTIC, we find that asymmetry of the electrode does not play any role in improving the performance of SSTICs because the temperature difference across the device is very small, and one is in the linear regime. The most important parameter seems to be the energy barrier height, and the structure with the lowest barrier height (0.10 eV) shows the highest performance. Finally, we estimated the electron MFP at the Fermi level and across the MoSe₂ planes to be 200 and 35 Å at 300 and 1000 K, respectively, which is larger than the thickness of the structures considered here.

ACKNOWLEDGMENTS

This paper is supported by the National Science Foundation Grant No. 1653268. M.G.R. and K.E. acknowledge support from Hobby funding. The authors wish to acknowledge the Rivanna High-Performance Computing system of the University of Virginia and Extreme Science and Engineering Discovery Environment.

- [1] A. Shakouri and J. E. Bowers, Heterostructure integrated thermionic coolers, *Appl. Phys. Lett.* **71**, 1234 (1997).
 [2] G. D. Mahan, J. O. Sofo, and M. Bartkowiak, Multilayer thermionic refrigerator and generator, *J. Appl. Phys.* **83**, 4683 (1998).

- [3] M. Markov and M. Zebarjadi, Thermoelectric transport in graphene and 2D layered materials, *Nanoscale Microscale Thermophys. Eng.* **23**, 117 (2019).
 [4] Y. Hishinuma, T. H. Geballe, B. Y. Mozyshes, and T. W. Kenny, Refrigeration by combined tunneling and thermionic emission

- in vacuum: Use of nanometer scale design, *Appl. Phys. Lett.* **78**, 2572 (2001).
- [5] M. G. Rosul, D. Lee, D. H. Olson, N. Liu, X. Wang, P. E. Hopkins, K. Lee, and M. Zebarjadi, Thermionic transport across gold-graphene-WSe₂ van der Waals heterostructures, *Sci. Adv.* **5**, eaax7827 (2019).
- [6] M. G. Rosul, M. S. Akhanda, and M. Zebarjadi, Thermionic energy conversion, in *Nanoscale Energy Transport: Emerging Phenomena, Methods and Applications*, edited by B. Liao (IOP Publishing, Bristol, 2020), pp. 14-1–14-29.
- [7] G. D. Mahan and L. M. Woods, Multilayer Thermionic Refrigeration, *Phys. Rev. Lett.* **80**, 4016 (1998).
- [8] M. Zebarjadi, Solid-State Thermionic Power Generators: An Analytical Analysis in the Nonlinear Regime, *Phys. Rev. Appl.* **8**, 014008 (2017).
- [9] Q. Li, Q. Hao, T. Zhu, M. Zebarjadi, and K. Takahashi, Nanostructured and heterostructured 2D materials for thermoelectrics, *Eng. Sci.* **13**, 24 (2020).
- [10] A. Ziabari, M. Zebarjadi, D. Vashae, and A. Shakouri, Nanoscale solid-state cooling: A review, *Rep. Prog. Phys.* **79**, 095901 (2016).
- [11] G. D. Mahan, Thermionic refrigeration, *J. Appl. Phys.* **76**, 4362 (1994).
- [12] A. K. Geim and I. V. Grigorieva, Van der Waals heterostructures, *Nature (London)* **499**, 419 (2013).
- [13] J. E. Padilha, A. Fazzio, and A. J. R. da Silva, Van der Waals Heterostructure of Phosphorene and Graphene: Tuning the Schottky Barrier and Doping by Electrostatic Gating, *Phys. Rev. Lett.* **114**, 066803 (2015).
- [14] A. L. Moore and L. Shi, Emerging challenges and materials for thermal management of electronics, *Mater. Today* **17**, 163 (2014).
- [15] X. Wang, M. Zebarjadi, and K. Esfarjani, First principles calculations of solid-state thermionic transport in layered van der Waals heterostructures, *Nanoscale* **8**, 14695 (2016).
- [16] X. Wang, M. Zebarjadi, and K. Esfarjani, High-performance solid-state thermionic energy conversion based on 2D van der Waals heterostructures: A first-principles study, *Sci. Rep.* **8**, 9303 (2018).
- [17] P. Yuan, C. Li, S. Xu, J. Liu, and X. Wang, Interfacial thermal conductance between few to tens of layered-MoS₂ and c-Si: effect of MoS₂ thickness, *Acta Mater.* **122**, 152 (2017).
- [18] S. Vaziri, E. Yalon, M. Muñoz Rojo, S. V. Suryavanshi, H. Zhang, C. J. McClellan, C. S. Bailey, K. K. H. Smithe, A. J. Gabourie, V. Chen, S. Deshmukh, L. Bendersky, A. V. Davydov, and E. Pop, Ultrahigh thermal isolation across heterogeneously layered two-dimensional materials, *Sci. Adv.* **5**, eaax1325 (2019).
- [19] M. Massicotte, P. Schmidt, F. Vialla, K. Watanabe, T. Taniguchi, K. J. Tielrooij, and F. H. L. Koppens, Photo-thermionic effect in vertical graphene heterostructures, *Nat. Commun.* **7**, 12174 (2016).
- [20] S.-J. Liang, B. Liu, W. Hu, K. Zhou, and L. K. Ang, Thermionic energy conversion based on graphene van der Waals heterostructures, *Sci. Rep.* **7**, 46211 (2017).
- [21] C.-C. Chen, Z. Li, L. Shi, and S. B. Cronin, Thermoelectric transport across graphene/hexagonal boron nitride/graphene heterostructures, *Nano Res.* **8**, 666 (2015).
- [22] N. Poudel, S.-J. Liang, D. Choi, B. Hou, L. Shen, H. Shi, L. K. Ang, L. Shi, and S. Cronin, Cross-plane thermoelectric and thermionic transport across Au/h-BN/graphene heterostructures, *Sci. Rep.* **7**, 14148 (2017).
- [23] N. Flöry, A. Jain, P. Bharadwaj, M. Parzefall, T. Taniguchi, K. Watanabe, and L. Novotny, A WSe₂/MoSe₂ heterostructure photovoltaic device, *Appl. Phys. Lett.* **107**, 123106 (2015).
- [24] G. Kioseoglou, A. T. Hanbicki, M. Currie, A. L. Friedman, and B. T. Jonker, Optical polarization and intervalley scattering in single layers of MoS₂ and MoSe₂, *Sci. Rep.* **6**, 25041 (2016).
- [25] W. S. Yun, S. W. Han, S. C. Hong, I. G. Kim, and J. D. Lee, Thickness and strain effects on electronic structures of transition metal dichalcogenides: 2H-MX₂ semiconductors ($M = \text{Mo, W}$; $X = \text{S, Se, Te}$), *Phys. Rev. B* **85**, 033305 (2012).
- [26] F. Léonard and A. A. Talin, Size-Dependent Effects on Electrical Contacts to Nanotubes and Nanowires, *Phys. Rev. Lett.* **97**, 026804 (2006).
- [27] Y.-F. Lin and W.-B. Jian, The impact of nanocontact on nanowire based nanoelectronics, *Nano Lett.* **8**, 3146 (2008).
- [28] J. Kang, W. Liu, D. Sarkar, D. Jena, and K. Banerjee, Computational Study of Metal Contacts to Monolayer Transition-Metal Dichalcogenide Semiconductors, *Phys. Rev. X* **4**, 031005 (2014).
- [29] J.-R. Chen, P. M. Odenthal, A. G. Swartz, G. C. Floyd, H. Wen, K. Y. Luo, and R. K. Kawakami, Control of Schottky barriers in single layer MoS₂ transistors with ferromagnetic contacts, *Nano Lett.* **13**, 3106 (2013).
- [30] S. Das, H.-Y. Chen, A. V. Penumatcha, and J. Appenzeller, High performance multilayer MoS₂ transistors with scandium contacts, *Nano Lett.* **13**, 100 (2013).
- [31] M. Fontana, T. Deppe, A. K. Boyd, M. Rinzan, A. Y. Liu, M. Paranjape, and P. Barbara, Electron-hole transport and photovoltaic effect in gated MoS₂ Schottky junctions, *Sci. Rep.* **3**, 1634 (2013).
- [32] M. Farmanbar and G. Brocks, Controlling the Schottky barrier at MoS₂/metal contacts by inserting a BN monolayer, *Phys. Rev. B* **91**, 161304(R) (2015).
- [33] M. Bokdam, G. Brocks, M. I. Katsnelson, and P. J. Kelly, Schottky barriers at hexagonal boron nitride/metal interfaces: a first-principles study, *Phys. Rev. B* **90**, 085415 (2014).
- [34] M. Bokdam, G. Brocks, and P. J. Kelly, Large potential steps at weakly interacting metal-insulator interfaces, *Phys. Rev. B* **90**, 201411(R) (2014).
- [35] C. P. Y. Wong, C. Troade, A. T. S. Wee, and K. E. J. Goh, Gaussian Thermionic Emission Model for Analysis of Au/MoS₂ Schottky-Barrier Devices, *Phys. Rev. Appl.* **14**, 054027 (2020).
- [36] H. Moss, Thermionic diodes as energy converters, *J. Electron. Control* **2**, 305 (1957).
- [37] V. C. Wilson, Conversion of heat to electricity by thermionic emission, *J. Appl. Phys.* **30**, 475 (1959).
- [38] H. F. Webster, Calculation of the performance of a high-vacuum thermionic energy converter, *J. Appl. Phys.* **30**, 488 (1959).
- [39] J. M. Soler, E. Artacho, J. D. Gale, A. García, J. Junquera, P. Ordejón, and D. Sánchez-Portal, The SIESTA method for *ab initio* order- N materials simulation, *J. Phys. Condens. Matter* **14**, 2745 (2002).
- [40] J. P. Perdew, K. Burke, and M. Ernzerhof, Generalized Gradient Approximation Made Simple, *Phys. Rev. Lett.* **77**, 3865 (1996).
- [41] J. P. Perdew, A. Ruzsinszky, G. I. Csonka, O. A. Vydrov, G. E. Scuseria, L. A. Constantin, X. Zhou, and K. Burke, Restoring the Density-Gradient Expansion for Exchange in Solids and Surfaces, *Phys. Rev. Lett.* **100**, 136406 (2008).

- [42] C. Huang, S. Wu, A. M. Sanchez, J. J. P. Peters, R. Beanland, J. S. Ross, P. Rivera, W. Yao, D. H. Cobden, and X. Xu, Lateral heterojunctions within monolayer MoSe₂-WSe₂ semiconductors, *Nat. Mater.* **13**, 1096 (2014).
- [43] F. A. Rasmussen and K. S. Thygesen, Computational 2D materials database: Electronic structure of transition-metal dichalcogenides and oxides, *J. Phys. Chem. C* **119**, 13169 (2015).
- [44] P. B. James and M. T. Lavik, The crystal structure of MoSe₂, *Acta Crystallogr.* **16**, 1183 (1963).
- [45] S. Nayeib Sadeghi, M. Zebarjadi, and K. Esfarjani, Non-linear enhancement of thermoelectric performance of a TiSe₂ monolayer due to tensile strain, from first-principles calculations, *J. Mater. Chem. C* **7**, 7308 (2019).
- [46] A. P. Nayak, S. Bhattacharyya, J. Zhu, J. Liu, X. Wu, T. Pandey, C. Jin, A. K. Singh, D. Akinwande, and J.-F. Lin, Pressure-induced semiconducting to metallic transition in multilayered molybdenum disulphide, *Nat. Commun.* **5**, 3731 (2014).
- [47] M. Dion, H. Rydberg, E. Schröder, D. C. Langreth, and B. I. Lundqvist, Van der Waals Density Functional for General Geometries, *Phys. Rev. Lett.* **92**, 246401 (2004).
- [48] J. Klimeš, D. R. Bowler, and A. Michaelides, Van der Waals density functionals applied to solids, *Phys. Rev. B* **83**, 195131 (2011).
- [49] M. Brandbyge, J.-L. Mozos, P. Ordejón, J. Taylor, and K. Stokbro, Density-functional method for nonequilibrium electron transport, *Phys. Rev. B* **65**, 165401 (2002).
- [50] K. Esfarjani, M. Zebarjadi, and Y. Kawazoe, Thermoelectric properties of a nanocontact made of two-capped single-wall carbon nanotubes calculated within the tight-binding approximation, *Phys. Rev. B* **73**, 085406 (2006).
- [51] P. Giannozzi, S. Baroni, N. Bonini, M. Calandra, R. Car, C. Cavazzoni, D. Ceresoli, G. L. Chiarotti, M. Cococcioni, I. Dabo, A. Dal Corso, S. de Gironcoli, S. Fabris, G. Fratesi, R. Gebauer, U. Gerstmann, C. Gougoussis, A. Kokalj, M. Lazzeri, L. Martin-Samos *et al.*, QUANTUM ESPRESSO: a modular and open-source software project for quantum simulations of materials, *J. Phys. Condens. Matter* **21**, 395502 (2009).
- [52] N. Troullier and J. L. Martins, Efficient pseudopotentials for plane-wave calculations, *Phys. Rev. B* **43**, 1993 (1991).
- [53] S. Poncé, E. R. Margine, C. Verdi, and F. Giustino, EPW: electron-phonon coupling, transport and superconducting properties using maximally localized Wannier functions, *Comput. Phys. Commun.* **209**, 116 (2016).
- [54] F. Giustino, M. L. Cohen, and S. G. Louie, Electron-phonon interaction using Wannier functions, *Phys. Rev. B* **76**, 165108 (2007).
- [55] G. K. H. Madsen and D. J. Singh, BOLTZTRAP. A code for calculating band-structure dependent quantities, *Comput. Phys. Commun.* **175**, 67 (2006).
- [56] See Supplemental Material at <http://link.aps.org/supplemental/10.1103/PhysRevB.105.115412> for the transmission function of the Au, Pt, Cu, and Ni symmetric structures; the thermal transmission window of the Cu structure with five layers of MoSe₂; a breakdown of PFT of 3–6 layers of Au-MoSe₂-Au structure for a different temperature range; the SSTIC performance of a gold-platinum symmetric and asymmetric structure with three layers of MoSe₂; the SSTIC performance comparison of a Cu-3 MoSe₂-Cu and Cu-5 MoSe₂-Cu structure; the electron-phonon scattering rate and MFP of bulk MoSe₂; and the band structure of bulk and 1–5 layers of MoSe₂.
- [57] A. Rawat, N. Jena, D. Dimple, and A. De Sarkar, A comprehensive study on carrier mobility and artificial photosynthetic properties in group VI B transition metal dichalcogenide monolayers, *J. Mater. Chem. A* **6**, 8693 (2018).
- [58] Z. Li, S. R. Bauers, N. Poudel, D. Hamann, X. Wang, D. S. Choi, K. Esfarjani, L. Shi, D. C. Johnson, and S. B. Cronin, Cross-plane Seebeck coefficient measurement of misfit layered compounds (SnSe)_n(TiSe₂)_n ($n = 1, 3, 4, 5$), *Nano Lett.* **17**, 1978 (2017).